The Key Role of Cloud–Climate Coupling in Extratropical Sea Surface Temperature Variability

Chloe L. Boehm[a] and David W. J. Thompson[a,b]

[a] Department of Atmospheric Science, Colorado State University, Fort Collins, Colorado
[b] School of Environmental Sciences, University of East Anglia, Norwich, United Kingdom

(Manuscript received 12 May 2022, in final form 16 December 2022)

ABSTRACT: Cloud radiative effects have long been known to play a key role in governing the mean climate. In recent years, it has become clear that they also contribute to climate variability in the tropics. Here we build on recent work and probe the role of cloud radiative effects in extratropical sea surface temperature (SST) variability. The impact of cloud radiative effects on climate variability is explored in "cloud-locking" simulations run on an Earth System Model. The method involves comparing the output from two climate simulations: one in which clouds are coupled to atmospheric dynamic and thermodynamic processes, and another in which clouds are prescribed and thus decoupled from them. The results reveal that cloud–climate coupling leads to widespread increases in the amplitudes of extratropical SST variability from monthly to decadal time scales. Notably, it leads to ~40%–100% increases in the amplitude of monthly to decadal variability over both the North Atlantic and North Pacific Oceans. These increases are consistent with the "reddening" of cloud shortwave radiative effects that arises when clouds respond to the dynamic and thermodynamic state of the atmosphere. The results suggest that a notable fraction of observed Northern Hemisphere SST variability—including that associated with North Pacific and North Atlantic decadal variability—is due to cloud–climate coupling.

KEYWORDS: North Atlantic Ocean; North Pacific Ocean; Sea surface temperature; Cloud radiative effects; Climate variability; Decadal variability

1. Introduction

Clouds and their radiative effects play an essential role in governing the mean climate (e.g., Stephens et al. 2012 and references therein). They give rise to some of the most important—and most uncertain—feedbacks under climate change (e.g., Bony and Dufresne 2005; Zelinka and Hartmann 2010; Bony et al. 2015; Sherwood et al. 2020 and references therein), and they play an important role in the dynamical response to climate change (e.g., Voigt and Shaw 2015, 2016; Ceppi and Hartmann 2016; Albern et al. 2018, 2019, 2020; Grise et al. 2019; Voigt and Albern 2019; Voigt et al. 2021 and references therein). In recent years, it has become increasingly clear that they also play an important role in climate variability.

The role of clouds in climate variability has been investigated primarily in the tropics. In particular, cloud radiative effects are believed to play an important role in governing variability in the El Niño–Southern Oscillation (ENSO) phenomenon (Rädel et al. 2016; Middlemas et al. 2019). The coupling between cloud radiative effects and ENSO is theorized to arise from the influence of longwave cloud radiative effects on the amplitude of the feedbacks between east–west gradients in heating and the zonal flow (e.g., Rädel et al. 2016). The importance of cloud radiative effects for extratropical variability is generally less clear, and most studies have focused on their role in relatively short-term dynamic variability (Li et al. 2014; Schäfer and Voigt 2018; Grise et al. 2019; Papavasileiou et al. 2020).

In a recent paper (Li et al. 2020), we argued that the role of cloud radiative effects in tropical climate variability extends beyond their influence on the ENSO phenomenon. We suggested that the primary role of cloud–climate coupling in climate variability is to enhance the persistence of surface shortwave radiative fluxes—and thus of surface temperatures—throughout the tropics. However, Li et al. (2020) focused primarily on results in tropical regions. Here we extend that paper to probe the role of cloud radiative effects in sea surface temperature (SST) variability in *extratropical* regions. The key conclusion is that—at least in an Earth System Model—coupling between cloud radiative effects and atmospheric dynamic and thermodynamic processes leads to substantial increases in the amplitude of Northern Hemisphere SST variability on time scales ranging from months to decades. Cloud–climate coupling thus appears to play an important role in the most important patterns of extratropical multidecadal climate variability in the North Atlantic and North Pacific sectors. Section 2 reviews the numerical experiments and analysis technique. Section 3 explores the role of cloud radiative effects in extratropical SST variability in the numerical output. Section 4 provides an interpretation of the results, and section 5 reviews the key conclusions.

2. Output and methods

The role of cloud radiative effects in extratropical SST variability is quantified by comparing output from two simulations run on a fully coupled Earth System Model: an "interactive" or control simulation where cloud radiative effects are coupled to

Corresponding author: Chloe L. Boehm, chloe.boehm@colostate.edu

DOI: 10.1175/JCLI-D-22-0362.1

the dynamic and thermodynamic state of the atmosphere; and a "locked" simulation where cloud radiative effects are decoupled from it. Thus, comparing the interactive and locked simulations allows us to explicitly explore the role of cloud–climate coupling in climate variability. Variations of the cloud-locking technique applied here have been exploited in numerous previous studies, including Voigt and Shaw (2015, 2016), Ceppi and Hartmann (2016), Rädel et al. (2016), Middlemas et al. (2019) and Olonscheck et al. (2019). The experiments used here were conducted by D. Olonscheck at the Max Planck Institute for Meteorology (MPI) and are identical to those described in detail in Li et al. (2020). A brief summary of the experiments is provided below. For a more detailed review of the experiment design, the reader is referred to the companion study (Li et al. 2020).

The simulations were run on the Max Planck Institute Earth System Model (MPI-ESM) at T63 (200-km) horizontal resolution and with 47 vertical levels in the atmosphere, and at 1.5° (150-km) horizontal resolution and with 40 vertical levels in the ocean. The resolution of the ocean model does not permit explicitly resolved ocean mesoscale eddies, but for reasons that will become clear later, we see no reason the model ocean resolution should affect the conclusions of the study. The interactive simulation was run for 250 years with preindustrial forcing, but we use only the last 200 years of the simulation to account for model spinup. The locked simulation was performed in the same way, except that all cloud parameters were randomized before being read into the radiation code. The randomization was accomplished by 1) saving cloud parameters at every 2-h radiation call from the interactive simulation; 2) randomizing the order of the years but not the hours or days associated with the cloud properties at each time step; and 3) reading the randomized cloud fields into the radiation code at every 2-h time step when running the locked simulation. As such, the cloud parameters in the locked simulation have the same long-term mean diurnal and seasonal cycles as those in the interactive simulation, but they are decoupled from variability in the atmosphere on all time scales. Note that scrambling the order of the years ensures that there is no memory—and thus no autocorrelation—in the cloud fields from one time step to the next. For details on the locking methodology, see Rädel et al. (2016) and Olonscheck et al. (2019). For discussion of the different scrambling methods used in various cloud-locking experiments, see Li et al. (2020).

The changes in SST variability between the interactive and locked simulations are expressed as percent changes in variance $[(s_i^2/s_l^2) - 1] \times 100$, where s_i^2 and s_l^2 denote the variances from the interactive and locked runs, respectively. The linear trend and seasonal cycle of the SST and surface flux fields are removed before all analyses. Time filtering is done using a Butterworth filter. Statistical significance of the variance ratios is found using the F statistic, where $F = (s_i^2/s_l^2)$.

All variance ratios are tested at the 95% confidence level where the degrees of freedom are estimated from the autocorrelation as per Leith (1973). That is: 1) the e-folding time scale is defined at each grid point as the time step where the autocorrelation drops below $1/e$ and then 2) the effective sample size is found as $N^* = N/(2T_e)$, where N^* is the effective sample size, N is the number of months, and T_e is the e-folding time scale. For example, in the extratropical North Pacific, the e-folding time scale of unfiltered monthly mean output is ~10 months, which leads to roughly 2400/20 or ~120 degrees of freedom across all 2400 time steps in the output (recall the analyses are based on 200 years of monthly resolved output). In contrast, the e-folding time scale for 10-yr low-pass-filtered output is ~50 months, which leads to roughly 2160/100 or ~20 degrees of freedom across all 2160 time steps in the output. Note that the Leith (1973) method is considerably more conservative than that proposed in Bretherton et al. (1999). Note also that the unfiltered and low-pass-filtered datasets are of different lengths since the filtering leads to a loss of output at the beginning and end of the time series.

As noted in Olonscheck et al. (2019) and Li et al. (2020), the MPI-ESM locked simulations exhibit weak increases in climatological-mean surface temperatures at polar latitudes, especially in regions with sea ice coverage. Due to this warm bias in the cloud-locking simulation, we focus on results between 60°S and 70°N and thus exclude regions where the bias might influence the results. As shown in appendix A (see Fig. A1), the variability of the SST field in the MPI-ESM interactive simulation is comparable to that found in ERA5 output (Hersbach et al. 2020).

3. The contribution of cloud–climate coupling to extratropical SST variability

Figures 1–5 compare the variability of SST anomalies in the interactive and locked simulations.

The climatological standard deviations from the interactive and locked runs are shown in the left and middle panels of Fig. 1, respectively. In both simulations, the largest standard deviations are found over the Gulf Stream and Kuroshio regions, locations where both the horizontal gradients in the surface temperature field and ocean heat transport contribute to large SST variability. The percent *changes* in the variances between the interactive and locked runs {i.e., $[(s_i^2/s_l^2) - 1] \times 100$} are shown in Fig. 1c. Stippling in Fig. 1c indicates regions where the associated variance ratios (s_i^2/s_l^2) are statistically significant at the 95% confidence level using the F statistic (section 2).

The most widespread changes in SST variability are found in the tropics, where cloud–climate coupling leads to increases in the variance of SSTs of ~100%–200% over most of the tropical oceans. As noted in the Introduction, changes in tropical SST variability due to cloud–climate coupling have been explored in several previous studies, including the companion study (Li et al. 2020). However, Fig. 1c also reveals widespread increases in variance over the western North Pacific and western North Atlantic basins. These regions were not explored in Li et al. (2020) and are the focus here.

The increases in SST variability over the North Pacific and North Atlantic basins are apparent in monthly mean output (Fig. 1c), but are particularly pronounced in output filtered to remove variability on time scales shorter than 1, 3, and 10 years (Fig. 2). The results based on 3- and 10-yr low-pass-filtered output are derived from a smaller sample size due to the filtering (section 2), but nevertheless indicate significant increases over

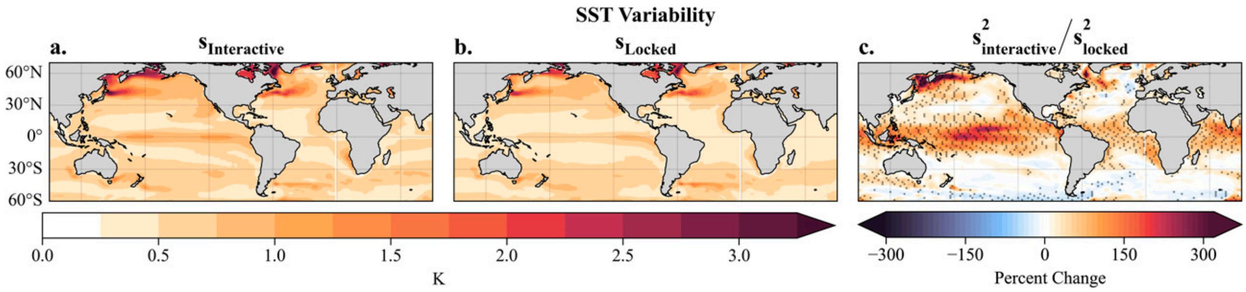

FIG. 1. Monthly mean SST standard deviation for (a) the 200-yr interactive simulation and (b) the 200-yr locked simulation. (c) The ratios of SST variances between the interactive and locked simulations expressed as percent change. Stippling indicates where the SST variance ratio between the simulations is statistically significant at the 95% confidence level using the F statistic (see section 2). Results are analogous to those shown in Fig. 1 of Li et al. (2020).

large regions of the Northern Hemisphere extratropical oceans, particularly the western halves of the basins. The increases in decadal SST variability due to cloud–climate coupling are ~50%–200% over most of the Northern Hemisphere Oceans (Fig. 2c). The changes in the Southern Ocean are weak, amorphous, and not statistically significant. With the exception of subpolar latitudes, the increases in Northern Hemisphere SST variability are less clear in output that has been 1-yr high-pass filtered (see Fig. B1 in appendix B). Thus, cloud–climate coupling appears to be most important for extratropical Northern Hemisphere SST variability on interannual and longer time scales.

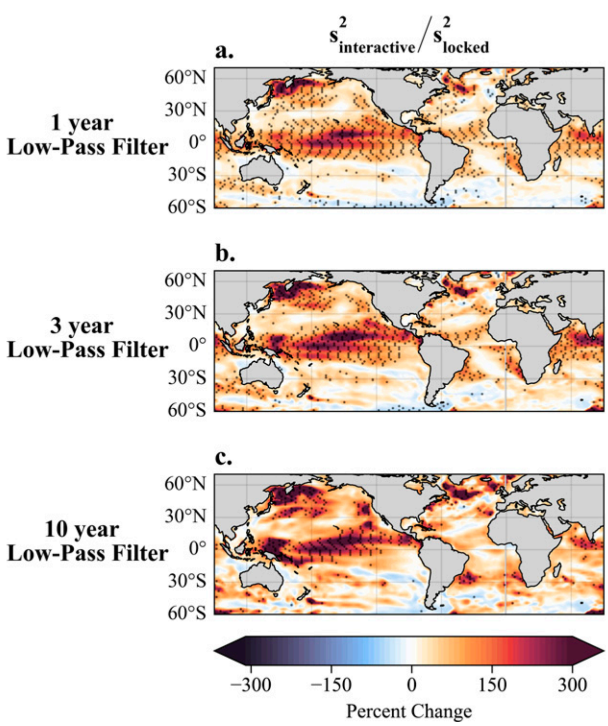

FIG. 2. The ratios of SST variances between the interactive and locked simulations expressed as percent change. (a) Temperatures have been 1-yr low-pass filtered. (b) Temperatures have been 3-yr low-pass filtered. (c) Temperatures have been 10-yr low-pass filtered. Stippling indicates where the SST variance ratio between the simulations is statistically significant at the 95% confidence level using the F statistic (see section 2).

The increases in SST variability due to cloud–climate coupling readily extend to results averaged over large spatial regions. The center panel in Fig. 3 reproduces the percent change in 3-yr low-pass-filtered temperature variability from Fig. 2b, and the surrounding panels show the changes in variance for SSTs that have been low-pass filtered (as indicated on the abscissas) and then averaged over large spatial regions (as indicated in the panel captions). For example, results at 2 years on the North Pacific panel (Fig. 3b) were found by 1) applying a 2-yr low-pass filter to the gridpoint output; 2) calculating the variances of the gridpoint output; 3) spatially averaging the variances over the North Pacific; and 4) calculating the percent changes in the spatially averaged variances between the interactive and locked output. Cloud–climate coupling leads to increases in area-mean variances over all regions and for all low-pass filters. The increases in variability are only ~25% over the Southern Ocean, but ~40%–60% over the North Atlantic, ~60%–100% over the North Pacific sector, and ~80%–125% in the tropics. Comparing the North Pacific to the tropical oceans, it is clear that cloud–climate coupling has a comparable effect on low-frequency time scales across both regions.

Figure 4 again reproduces the percent change in 3-yr low-pass-filtered temperature variability from Fig. 2b, but now the surrounding panels show the corresponding SST power spectra for each region. Power spectra are first calculated for each grid point and then averaged over the respective regions. The individual gridpoint power spectra are scaled so that the area under the curve is equal to the total SST variance at that grid point. The differences in the spectra between the interactive and locked simulations are readily apparent across all four regions.

Together, the results in Figs. 1–4 indicate that cloud–climate coupling contributes to surface temperature variability not only in the tropics, as shown in Li et al. (2020), but over much of the extratropical Northern Hemisphere ocean basins as well. That the increases extend to low-frequency time scales has implications for the interpretation of Northern Hemisphere decadal climate variability. For example, Fig. 5

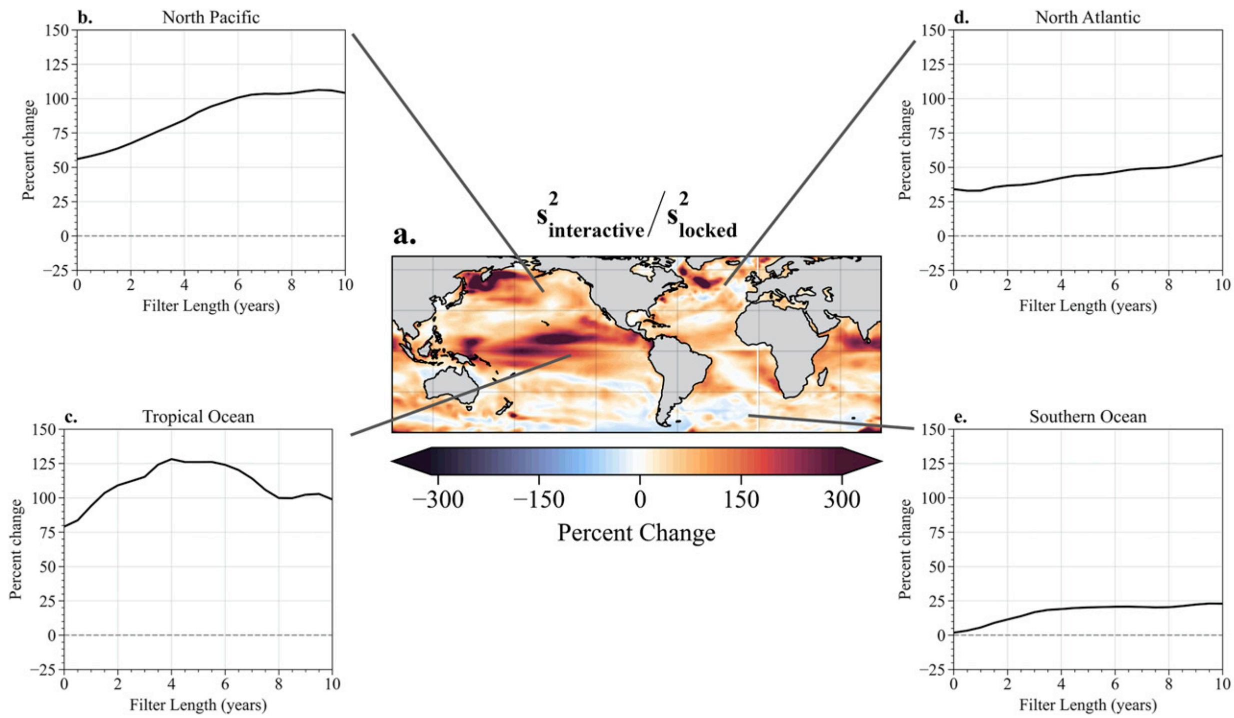

FIG. 3. Changes in SST variability for four different regions due to cloud–climate coupling. (a) Percent changes in 3-yr low-pass-filtered SST variance reproduced from Fig. 2b. Percent changes of the variances of SSTs for different low-pass-filtered lengths and averaged over (b) the North Pacific (15°–70°N, 129°–242°E), (c) the tropical ocean (15°S–15°N), (d) the North Atlantic (15°–70°N, 285°–360°E), and (e) the Southern Ocean (30°–60°S).

shows the time series commonly used to explore the two most prominent patterns of decadal variability in the Northern Hemisphere: the Atlantic multidecadal oscillation (AMO)/ Atlantic multidecadal variability (AMV) and the Pacific decadal oscillation (PDO). The indices are calculated by subtracting global-mean SST anomalies from spatially averaged North Atlantic and North Pacific SST anomalies, respectively. Cloud–climate coupling leads to ~100% and 130% increases in the variances of the AMO/AMV and PDO indices, respectively, both of which are significant at the 98% level based on the F statistic. The increases in variability of the AMO/AMV and PDO indices due to cloud–climate coupling are also visually apparent in the time series (cf. the left and right columns in Fig. 5). The doubling of the amplitudes of the AMO/AMV and PDO due to cloud–climate coupling indicates a potentially important but largely overlooked source of Northern Hemisphere decadal variability.

Finally, Fig. 6 explores whether the changes in SST variance extend to the tropospheric circulation. The left and middle panels show the standard deviations of 500-hPa geopotential height for the locked and interactive simulations, respectively, and the right panel shows the percent changes between the two simulations. In general, there are large and significant increases in the variance of 500-hPa geopotential heights throughout tropics (Fig. 6c), where the climatological-mean standard deviations are relatively small (Fig. 6a) and the increases in SST variability are most pronounced (Figs. 1 and 2). However, there are also scattered increases in the extratropics, in particular over the western North Pacific, some regions of the North Atlantic, and parts of the Southern Ocean. The increases in the extratropical Northern Hemisphere are relatively weak since the total standard deviations of 500-hPa geopotential height are very large there. But they are no less significant than their tropical counterparts. The changes in extratropical geopotential height variance could derive from 1) the remote response to cloud–climate coupling in the tropics or 2) the response to in situ changes in extratropical cloud–climate coupling. It would be interesting to test the relative roles of tropical and extratropical cloud–climate coupling in future experiments.

In the following section, we diagnose the physical factors responsible for the increases in extratropical SST variability. In section 5, we summarize the key conclusions.

4. Interpretation

Why does cloud–climate coupling lead to increased variability in extratropical SSTs? The diagnostic approach used to assess the key physical processes that underlie the changes in SST variability are reviewed in detail in Li et al. (2020) and are repeated here only briefly. In short, consider the thermodynamic energy equation at the surface:

$$C\frac{dT'}{dt} = \sum Q', \tag{1}$$

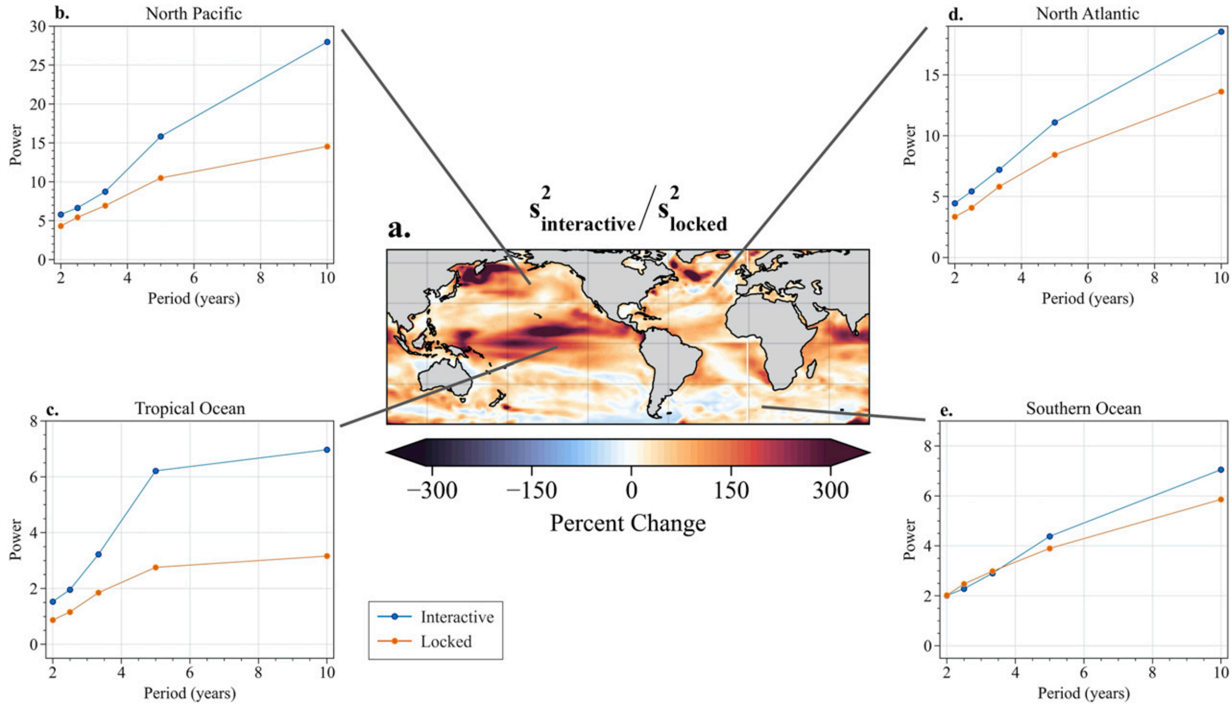

FIG. 4. Power spectra of SST anomalies for four different regions for the interactive and locked simulations. (a) Percent changes of 3-yr low-pass-filtered SST variance reproduced from Fig. 2b. Power spectra of SST anomalies for each simulation and averaged over (b) the North Pacific (15°–70°N, 129°–242°E), (c) the tropical ocean (15°S–15°N), (d) the North Atlantic (15°–70°N, 285°–360°E), and (e) the Southern Ocean (30°–60°S).

where C is the effective heat capacity of the ocean mixed layer, T' is the anomalous mixed-layer temperature (which is assumed to be linearly related to SSTs), and Q' denotes the various heat fluxes that influence variability in mixed-layer temperatures, including anomalies in the surface turbulent heat fluxes, the fluxes of shortwave and longwave radiation, and heat transport by the ocean circulation. In the following, Q' denotes the anomalies in the surface turbulent heat and radiative fluxes. We neglect anomalies in the horizontal ocean heat transport since—although ocean heat transport contributes significantly to the SST variance—it is not notably influenced by cloud–climate coupling in the MPI-ESM (Li et al. 2020).

The conversion of Eq. (1) into a diagnostic equation for the temperature variance involves 1) assuming all terms in Eq. (1) reflect departures from the long-term mean, 2) replacing the derivative with a centered differencing scheme, 3) squaring the resulting equation, and 4) taking the time average. The resulting expression for the temperature variance can be expressed as

$$\sigma_T^2 = G\sigma_\Sigma^2 e, \tag{2}$$

where σ_T^2 denotes the temperature variance; $\sigma_\Sigma^2 \equiv \sum Q'^2$ is the sum of the variances of the individual surface fluxes; $G = 2(\Delta t)^2/\{C^2[1 - r(2\Delta t)]\}$ is a "transfer term" that accounts for the influence of persistence on the variance estimate, where persistence is given by the lag-2-month autocorrelation $r(2\Delta t)$; and $e = 1 + (2\sum \overline{Q_i Q_j}/\sigma_\Sigma^2)$ is an "efficiency term" that accounts for the covariances between the individual surface fluxes, denoted by the i and j subscripts (i.e., negative correlations between different fluxes lead to $e < 1$).

The changes in temperature variances between the interactive and locked simulations can thus arise from changes in three ratios:

$$\frac{(\sigma_T^2)_i}{(\sigma_T^2)_l} = \frac{G_i}{G_l}\frac{(\sigma_\Sigma^2)_i}{(\sigma_\Sigma^2)_l}\frac{e_i}{e_l}. \tag{3}$$

Results for all three ratios on the rhs of Eq. (3) are shown in appendix C (see Fig. C1) and reveal the following: 1) The efficiency term [last term on the rhs of Eq. (3)] is slightly smaller in the interactive simulation (Fig. C1c), acting to reduce the effectiveness of the flux variances due to cross-correlations between the individual fluxes; 2) the transfer term (first term on the rhs) increases slightly between the locked and interactive simulations and mainly in the tropics (Fig. C1a), where the autocorrelation of the monthly mean extratropical SST field increases slightly (not shown); and 3) changes in the second term on the rhs are generally much larger than changes in the efficiency and transfer terms. Note that the efficiency term (last term on the rhs) and the sum of surface flux variances term (second term on the rhs) exhibit some compensation, since the former includes both the covariances and the sum of the variances. Nevertheless, as shown in Li et al. (2020), the increases in SST variances between the locked and interactive

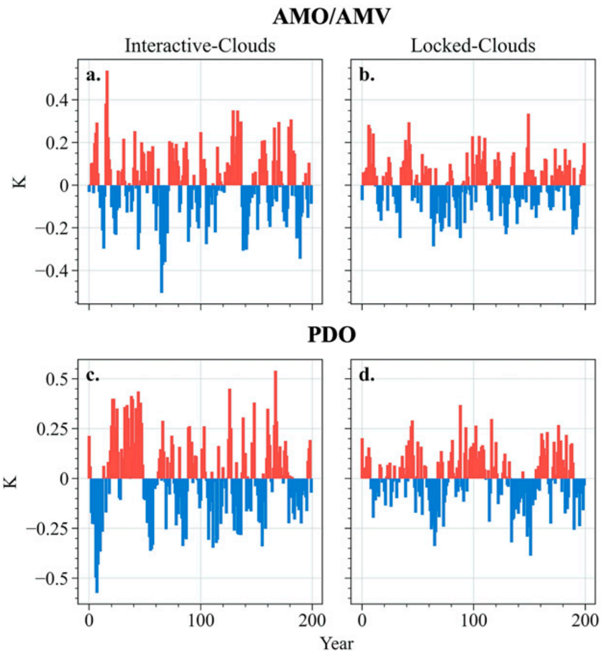

FIG. 5. Time series of the Atlantic multidecadal oscillation (AMO)/Atlantic multidecadal variability (AMV) and the Pacific decadal oscillation (PDO) for both the (a),(c) interactive and (b),(d) locked simulations. Indices are calculated by subtracting the global-mean anomalous SSTs (60°S–60°N) from the spatially averaged North Atlantic (0°–60°N, 279°–360°E) and North Pacific (20°–70°N, 129°–241°E) anomalous SSTs.

simulations are driven primarily by the increases in the surface flux variances (cf. Fig. C1b with Figs. C1a,c).

Figure 7 explores the specific fluxes responsible for the increases in the surface flux variances between the locked and interactive simulations. The first column shows the climatological-mean surface flux variances in the interactive simulation (we focus only on the surface heat fluxes since the changes in ocean heat transport are trivial between the interactive and locked simulations; Li et al. 2020). In general, the total variance of the fluxes is dominated by the latent, sensible, and shortwave radiative fluxes: The latent heat fluxes are dominant over the subtropical oceans, the sensible heat fluxes have the largest amplitudes over the western boundary current regions, and the radiative flux variances are more spatially amorphous. The second column shows the attendant climatological-mean surface flux variances in the locked simulation, and the third column shows the percent changes in the variances between the two simulations. By far the largest changes in surface fluxes between the interactive and locked simulations are found in association with the radiative fluxes, especially the shortwave fluxes (Figs. 7c,g). The increases in the shortwave radiative flux variances are prominent not only in the tropics but also across the extratropics. Hence, as is the case in the tropics (Li et al. 2020), the increases in surface temperature variance over both the North Atlantic and North Pacific due to cloud–climate coupling derive primarily from increases in the variance of shortwave fluxes.

Why does cloud–climate coupling increase the variance of the shortwave fluxes? In Li et al. (2020) we hypothesized that cloud–climate coupling acts to redden the power spectra of cloud fraction–and thus of cloud radiative effects—since the wind and temperature fields impart persistence to the cloud fields. Such persistence could arise from either internal atmospheric processes or the influence of ocean dynamics on the sea surface temperature field. In the absence of support from atmospheric thermodynamic and dynamic processes, clouds would presumably exhibit a much shorter lifespan. In the case of the simulations shown here, when the cloud fields are scrambled and thus decoupled from the atmosphere, the total variances of cloud fraction are preserved, but the variance is distributed roughly equally across all time scales since there is no memory in the cloud fields from one 2-h time step to the next. Thus, when clouds are decoupled from the atmosphere, the total variance of the cloud fields is preserved, but the variance on time scales longer than a few days decreases while the variance on time scales less than a few days increases. In short, when clouds are coupled to the atmosphere, the variance of cloud radiative effects increases on time scales longer than a few days, which, in turn, increases the variability of SSTs on the same time scales. As seen in Fig. 7c, this effect is particularly apparent in shortwave cloud radiative effects. Li et al. (2020) argue that the above mechanism is key in the

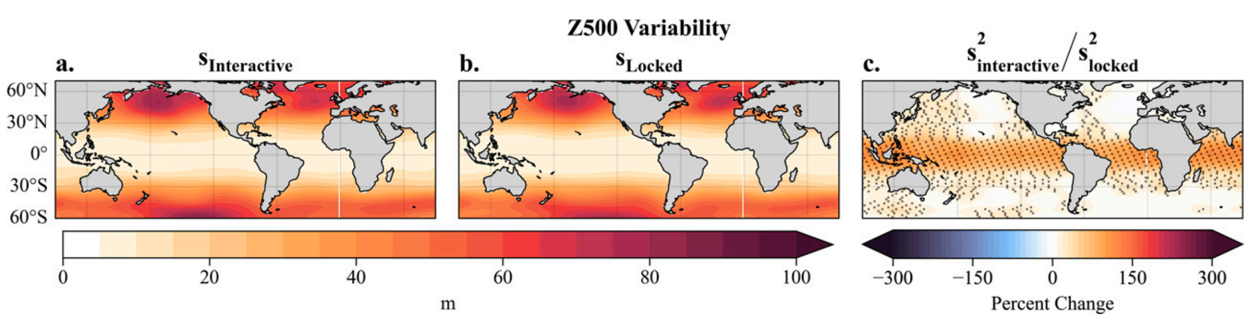

FIG. 6. Standard deviations of monthly mean anomalous geopotential height at 500 hPa (Z500) for (a) the 200-yr interactive simulation and (b) the 200-yr locked simulation. (c) The ratios of Z500 variances between the interactive and locked simulations expressed as percent change. Stippling indicates where the Z500 variance ratio between the simulations is statistically significant at the 95% confidence level using the F statistic (see section 2).

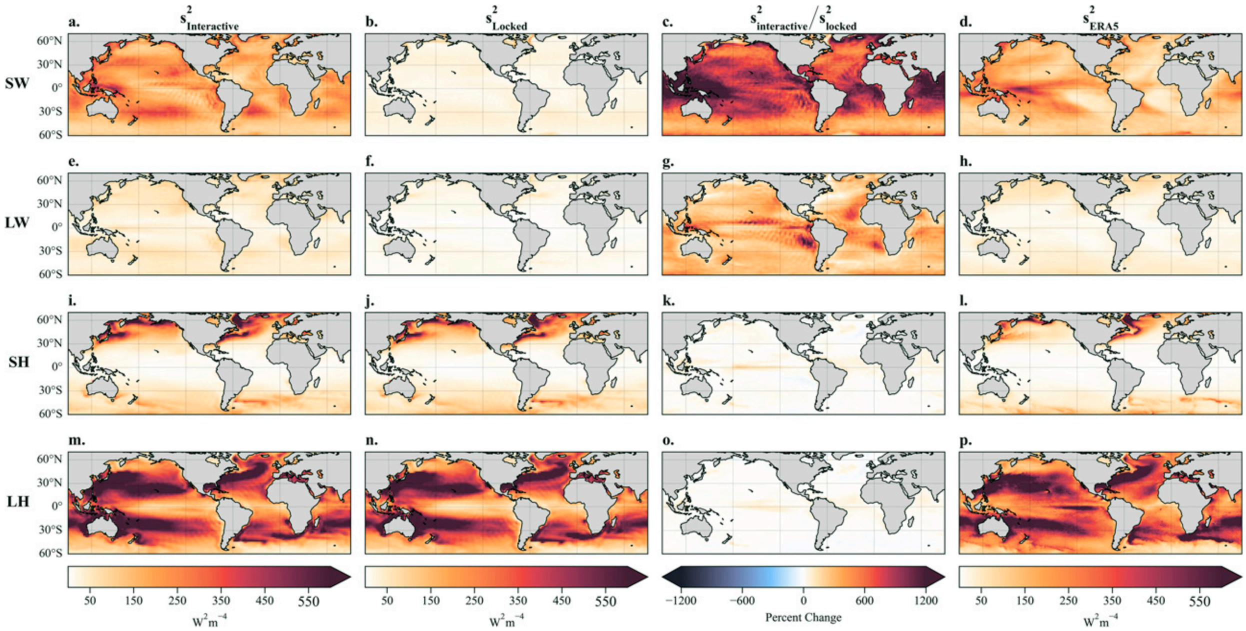

FIG. 7. Surface flux variances: (a)–(d) surface shortwave radiative flux, (e)–(h) surface longwave radiative flux, (i)–(l) surface sensible heat flux, and (m)–(p) surface latent heat flux. Individual flux variance for the (first column) interactive and (second column) locked simulations. (third column) Percent change of the individual surface flux variance between the interactive and locked simulations. (fourth column) Surface flux variances as estimated by ERA5. Results in the first and second columns are analogous to those shown in Fig. 4 of Li et al. (2020).

tropics; the results shown here suggest it is also key in the extratropics. The argument also holds for changes in longwave cloud radiative effects, but 1) the changes in the longwave flux variances shown in Fig. 7 conflate changes due to clouds and surface temperatures and 2) the changes in the longwave flux variances are smaller than the changes in the shortwave flux variances.

It is notable that cloud–climate coupling has a very small effect on surface temperature variance in the Southern Hemisphere extratropics, especially poleward of ~45°S. We hypothesize this is in part due to the nearly constant cloud cover over that area of the Southern Ocean (e.g., Mace and Zhang 2014; Mace and Protat 2018). Since there is a high incidence of cloud cover, it follows that decoupling clouds from the atmosphere has less effect on the variance of their radiative effects. This is most clear south of ~45°S where the changes in the variance of shortwave cloud radiative effects are relatively small (Fig. 7c).

5. Discussion

Together, the results shown here indicate that cloud–climate coupling has a pronounced effect on SST variability not only in the tropics—as indicated in previous work (Rädel et al. 2016; Middlemas et al. 2019; Li et al. 2020)—but also in the extratropics. Prominent increases in SST variability are found over the North Pacific and North Atlantic basins, where cloud–climate coupling increases the variance of SSTs by ~40%–100% on time scales ranging from months to decades. The changes in extratropical SST variability due to cloud–climate coupling were not appreciated in Li et al. (2020) since—in that study—we focused on the tropics and did not probe the amplitude and importance of the attendant changes in the extratropics.

The increases in extratropical SST variability appear to arise from the same mechanism that contributes to the increases in tropical SST variability. That is, cloud–climate coupling acts to "redden" the variance of clouds and their shortwave radiative effects, and thus enhances the contribution of cloud radiative effects to low-frequency climate variability. The increases in SST variability are accompanied by large increases in midtropospheric geopotential height variability in the tropics, and smaller but equally significant increases over the western North Pacific and scattered regions of the western North Atlantic. It remains unclear whether the changes in extratropical tropospheric geopotential height derive from the changes in cloud–climate coupling at tropical or extratropical latitudes. It also remains unclear whether the changes in SST variance derive entirely from one-way forcing of the SST field by changes in shortwave cloud radiative effects, or whether positive feedbacks between the SST field and shortwave CRE also play a role. It would be interesting to assess the relative importance of these aspects of the results in future work.

The results have potentially important implications for the interpretation and simulation of extratropical decadal variability. The variances of the surface fluxes in the interactive simulation bear very close resemblance to the observed fluxes, as estimated by ERA5 (cf. left and right columns in Fig. 7). Thus, in the real world, cloud–climate coupling may be viewed

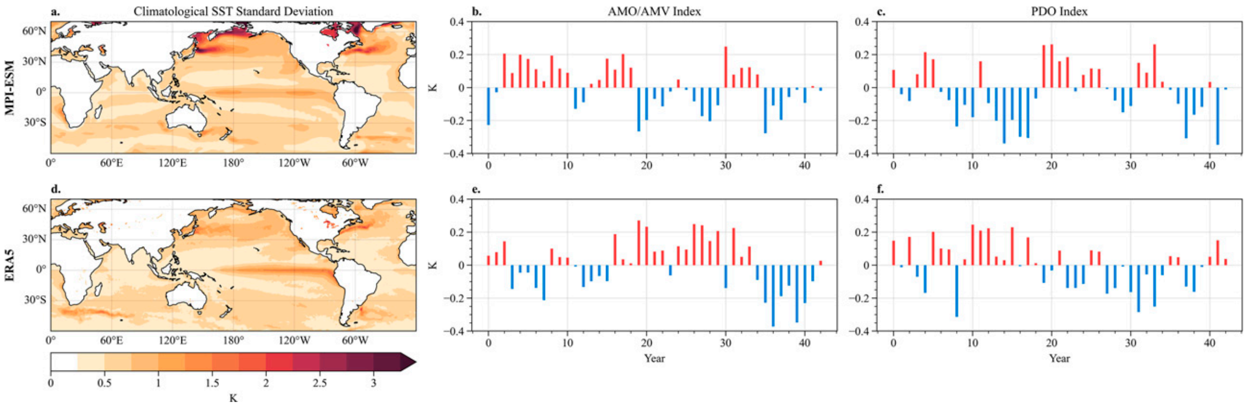

FIG. A1. Standard deviations of (a),(d) monthly mean SST anomalies; (b),(e) the AMO/AMV index time series; and (c),(f) the PDO index time series. Results are shown for the (top) 200-yr interactive simulation from the MPI-ESM and (bottom) as estimated by ERA5. Indices are calculated by subtracting the global-mean anomalous SSTs (60°S–60°N) from the spatially averaged North Atlantic (0°–60°N, 279°–360°E) and North Pacific (20°–70°N, 129°–241°E) anomalous SSTs.

as enhancing the variance of low-frequency temperature variability by roughly the same amount as found in the differences between the interactive and locked simulations. In particular, cloud–climate coupling leads to roughly a doubling in the variance of the most prominent patterns of low-frequency variability in the North Atlantic and North Pacific sectors, as indicated by time series of the AMO/AMV and the PDO.

The influence of cloud shortwave radiative effects on surface temperature variance shown here also has potentially important implications for the simulated amplitudes of internal climate feedbacks due to cloud–climate coupling. We defer analyses of the implications of the mechanism highlighted here for model feedbacks to future work.

Acknowledgments. We thank Dirk Olonscheck for providing the model output used in this and the companion study Li et al. (2020). We also thank Ying Li for analyses that provided the inspiration for exploring results on low-frequency time scales. Additionally, we acknowledge three anonymous reviewers for their helpful comments on the manuscript. CB and DWJT are supported by the NSF Climate and Large-Scale Dynamics Program. This work was supported by the NSF CLD Project Award 2055121.

Data availability statement. The cloud-locking simulation data used for the results of this study can be found online (http://dx.doi.org/10.25675/10217/234116; Boehm and Thompson 2021). The ERA5 output data are freely available online at: https://www.ecmwf.int/en/forecasts/datasets/reanalysis-datasets/era5.

APPENDIX A

Comparison of MPI-ESM to ERA5

Throughout this study we used SSTs from the Max Planck Institute Earth System Model (MPI-ESM). Figure A1 compares the standard deviations of SST anomalies along with the AMO/AMV and PDO indices between the MPI-ESM output and ERA5 output. Note that Fig. A1a is the same as Fig. 1a. Since the SST time series from the model is substantially longer than the available ERA5 output, we show only a randomly chosen subset of the model output of equal length to the reanalysis time series. As evidenced in Fig. A1, the modeled SST variability is qualitatively similar to that derived from the reanalysis, with the main exceptions found

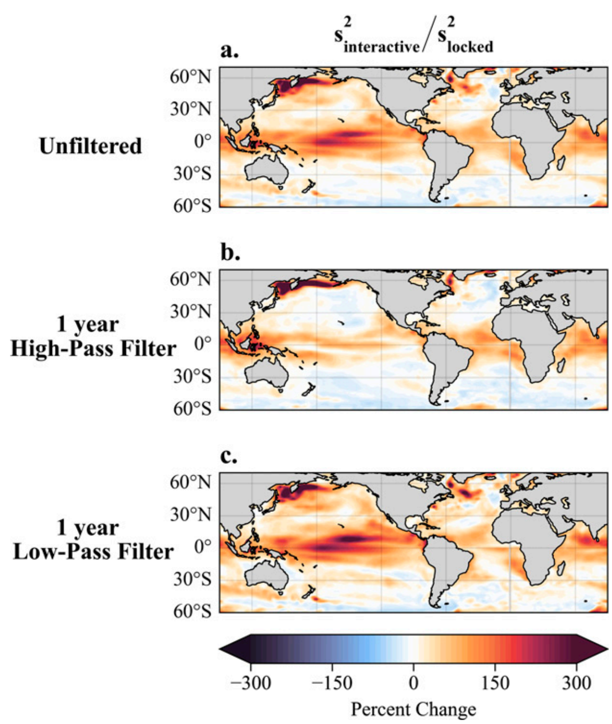

FIG. B1. The ratios of SST variances between the interactive and locked simulations expressed as percent change. (a) Temperature data are unfiltered (reproduced from Fig. 1c). (b) Temperatures have been 1-yr high-pass filtered. (c) Temperatures have been 1-yr low-pass filtered (reproduced from Fig. 2a).

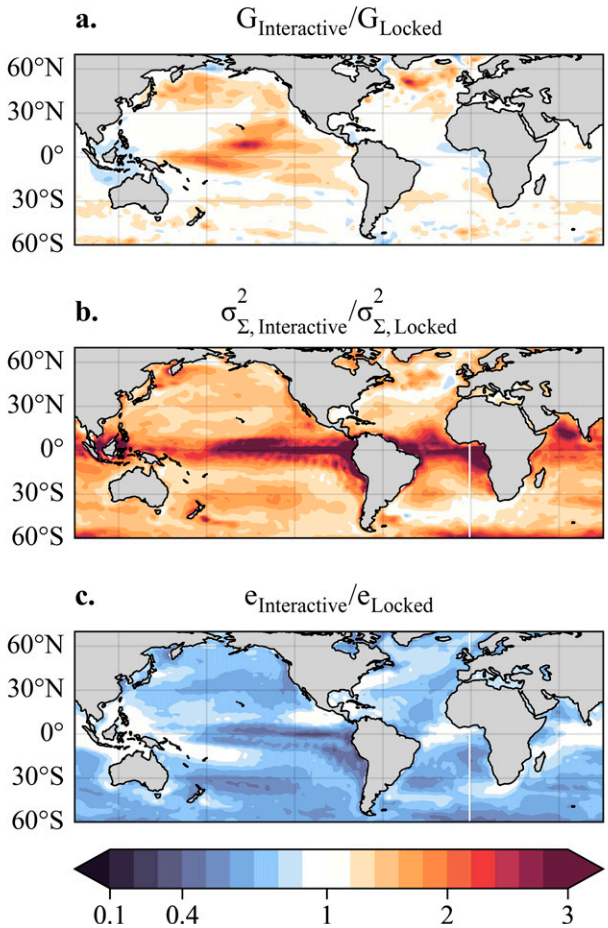

FIG. C1. The ratios of each term on the rhs of Eq. (3) calculated for the interactive and locked simulation. Results are analogous to those shown in Figs. 5c and C1 of Li et al. (2020), but do not include the effects of ocean advection.

in Northern Hemisphere subpolar regions and in the vicinity of the western boundary currents. Since the focus of our study is on the *differences* in variance between two ESM simulations, we do not expect differences in the control SST standard deviations to influence the conclusions.

APPENDIX B

The Impact of Cloud–Climate Coupling on High-Frequency SST Variability

Figure B1 compares the influence of cloud–climate coupling in 1-yr high-pass filtered output (middle panel) and 1-yr low-pass filtered output (bottom panel).

APPENDIX C

The Contribution of Individual Terms from the Diagnostic Equation to the Changes in Variance

Figure C1 shows the ratios of each term on the rhs of Eq. (3).

REFERENCES

Albern, N., A. Voigt, S. A. Buehler, and V. Grützun, 2018: Robust and nonrobust impacts of atmospheric cloud-radiative interactions on the tropical circulation and its response to surface warming. *Geophys. Res. Lett.*, **45**, 8577–8585, https://doi.org/10.1029/2018GL079599.

——, ——, and J. G. Pinto, 2019: Cloud-radiative impact on the regional responses of the midlatitude jet streams and storm tracks to global warming. *J. Adv. Model. Earth Syst.*, **11**, 1940–1958, https://doi.org/10.1029/2018MS001592.

——, ——, D. W. J. Thompson, and J. G. Pinto, 2020: The role of tropical, midlatitude, and polar cloud-radiative changes for the midlatitude circulation response to global warming. *J. Climate*, **33**, 7927–7943, https://doi.org/10.1175/JCLI-D-20-0073.1.

Boehm, C., and D. W. J. Thompson, 2021: Data associated with "The Key Role of Cloud-Climate Coupling in Extratropical Sea Surface Temperature Variability." Colorado State University, accessed 14 December 2021, https://doi.org/10.25675/10217/234116.

Bony, S., and J.-L. Dufresne, 2005: Marine boundary layer clouds at the heart of tropical cloud feedback uncertainties in climate models. *Geophys. Res. Lett.*, **32**, L20806, https://doi.org/10.1029/2005GL023851.

——, and Coauthors, 2015: Clouds, circulation and climate sensitivity. *Nat. Geosci.*, **8**, 261–268, https://doi.org/10.1038/ngeo2398.

Bretherton, C. S., M. Widmann, V. P. Dymnikov, J. M. Wallace, and I. Bladé, 1999: The effective number of spatial degrees of freedom of a time-varying field. *J. Climate*, **12**, 1990–2009, https://doi.org/10.1175/1520-0442(1999)012<1990:TENOSD>2.0.CO;2.

Ceppi, P., and D. L. Hartmann, 2016: Clouds and the atmospheric circulation response to warming. *J. Climate*, **29**, 783–799, https://doi.org/10.1175/JCLI-D-15-0394.1.

Grise, K. M., B. Medeiros, J. J. Benedict, and J. G. Olson, 2019: Investigating the influence of cloud radiative effects on the extratropical storm tracks. *Geophys. Res. Lett.*, **46**, 7700–7707, https://doi.org/10.1029/2019GL083542.

Hersbach, H., and Coauthors, 2020: The ERA5 global reanalysis. *Quart. J. Roy. Meteor. Soc.*, **146**, 1999–2049, https://doi.org/10.1002/qj.3803.

Leith, C. E., 1973: The standard error of time-average estimates of climatic means. *J. Appl. Meteor. Climatol.*, **12**, 1066–1069, https://doi.org/10.1175/1520-0450(1973)012<1066:TSEOTA>2.0.CO;2.

Li, Y., D. W. J. Thompson, Y. Huang, and M. Zhang, 2014: Observed linkages between the northern annular mode/North Atlantic oscillation, cloud incidence, and cloud radiative forcing. *Geophys. Res. Lett.*, **41**, 1681–1688, https://doi.org/10.1002/2013GL059113.

——, ——, and D. Olonscheck, 2020: A basic effect of cloud radiative effects on tropical sea surface temperature variability. *J. Climate*, **33**, 4333–4346, https://doi.org/10.1175/JCLI-D-19-0298.1.

Mace, G. G., and Q. Zhang, 2014: The CloudSat radar-lidar geometrical profile product (RL-GeoProf): Updates, improvements, and selected results. *J. Geophys. Res. Atmos.*, **119**, 9441–9462, https://doi.org/10.1002/2013JD021374.

——, and A. Protat, 2018: Clouds over the Southern Ocean as observed from the R/V investigator during CAPRICORN. Part I: Cloud occurrence and phase partitioning. *J. Appl. Meteor. Climatol.*, **57**, 1783–1803, https://doi.org/10.1175/JAMC-D-17-0194.1.

Middlemas, E. A., A. C. Clement, B. Medeiros, and B. Kirtman, 2019: Cloud radiative feedbacks and El Niño–Southern Oscillation. *J. Climate*, **32**, 4661–4680, https://doi.org/10.1175/JCLI-D-18-0842.1.

Olonscheck, D., T. Mauritsen, and D. Notz, 2019: Arctic sea-ice variability is primarily driven by atmospheric temperature fluctuations. *Nat. Geosci.*, **12**, 430–434, https://doi.org/10.1038/s41561-019-0363-1.

Papavasileiou, G., A. Voigt, and P. Knippertz, 2020: The role of observed cloud-radiative anomalies for the dynamics of the North Atlantic oscillation on synoptic time-scales. *Quart. J. Roy. Meteor. Soc.*, **146**, 1822–1841, https://doi.org/10.1002/qj.3768.

Rädel, G., T. Mauritsen, B. Stevens, D. Dommenget, D. Matei, K. Bellomo, and A. Clement, 2016: Amplification of El Niño by cloud longwave coupling to atmospheric circulation. *Nat. Geosci.*, **9**, 106–110, https://doi.org/10.1038/ngeo2630.

Schäfer, S. A. K., and A. Voigt, 2018: Radiation weakens idealized midlatitude cyclones. *Geophys. Res. Lett.*, **45**, 2833–2841, https://doi.org/10.1002/2017GL076726.

Sherwood, S. C., and Coauthors, 2020: An assessment of Earth's climate sensitivity using multiple lines of evidence. *Rev. Geophys.*, **58**, e2019RG000678, https://doi.org/10.1029/2019RG000678.

Stephens, G. L., and Coauthors, 2012: An update on Earth's energy balance in light of the latest global observations. *Nat. Geosci.*, **5**, 691–696, https://doi.org/10.1038/ngeo1580.

Voigt, A., and T. A. Shaw, 2015: Circulation response to warming shaped by radiative changes of clouds and water vapour. *Nat. Geosci.*, **8**, 102–106, https://doi.org/10.1038/ngeo2345.

——, and ——, 2016: Impact of regional atmospheric cloud radiative changes on shifts of the extratropical jet stream in response to global warming. *J. Climate*, **29**, 8399–8421, https://doi.org/10.1175/JCLI-D-16-0140.1.

——, and N. Albern, 2019: No cookie for climate change. *Geophys. Res. Lett.*, **46**, 14 751–14 761, https://doi.org/10.1029/2019GL084987.

——, ——, P. Ceppi, K. Grise, Y. Li, and B. Medeiros, 2021: Clouds, radiation, and atmospheric circulation in the present-day climate and under climate change. *Wiley Interdiscip. Rev.: Climate Change*, **12**, e694, https://doi.org/10.1002/wcc.694.

Zelinka, M. D., and D. L. Hartmann, 2010: Why is longwave cloud feedback positive? *J. Geophys. Res.*, **115**, D16117, https://doi.org/10.1029/2010JD013817.